Full length article

Block-based inverse lithography technology with adaptive level-set algorithm

Chaojun Huang [a], Xu Ma [a], Shengen Zhang [a], Mu Lin [a], Néstor Porras-Díaz [b], Gonzalo R. Arce [b]

[a] Key Laboratory of Photoelectronic Imaging Technology and System of Ministry of Education of China, School of Optics and Photonics, Beijing Institute of Technology, Beijing 100081, China
[b] Department of Electrical and Computer Engineering, University of Delaware, Newark, DE 19716, USA

ARTICLE INFO

ABSTRACT

Inverse lithography technology (ILT) is a key computational lithography approach aimed at inversely optimizing the photomask pattern to compensate for the image distortion in advanced optical lithography process. Traditional ILT algorithms, despite their capacity of significantly enhancing the image quality, bring challenges to the computational efficiency and mask manufacturability. To overcome those problems, this paper proposes a novel block-based ILT method driven by the level-set algorithm. This method leverages overlapped basis blocks with a level-set support area for mask representation, thus reducing the mask complexity. To circumvent the slow convergence rate dictated by the conventional Euler time step of the Courant-Friedrichs-Lewy condition, this research adopts the Barzilai-Borwein algorithm to update level set function using adaptive time step, which accelerates the optimization process. In addition, a testbed of digital lithography system is established to verify the proposed ILT method with a calibrated imaging model. It shows that the proposed method is superior over the widely-used and state-of-the-art ILT methods in terms of convergence speed and mask manufacturability.

1. Introduction

Optical lithography serves as a foundational and critical manufacturing process to fabricate very-large-scale integration circuits [1]. A schematic representation of the deep ultraviolet optical lithography system is provided in Fig. 1. This system employs Köhler illumination, which ensures that the light waves emitted from the 193 nm argon fluoride laser source are distributed uniformly over the mask. Then, the projection optics collects the diffracted light waves off the mask, focusing them onto the photoresist surface to form the aerial image. Finally, through a series of photoresist development processes, the print image is produced on the wafer.

However, as the critical dimensions (CD) of integration circuits continue to shrink, optical lithography faces increasing challenges due to the significant impact of diffraction and interference. These phenomena may lead to a serious mismatch between the print image and the target layout, undermining the imaging performance of optical lithography system. To compensate for the image distortions, a set of resolution enhancement techniques (RET) and computational lithography methods have been developed [2,3]. Computational lithography, in particular, employs mathematical models to simulate the optical lithography process [2], and utilizes numerical algorithms to optimize

the mask patterns, illumination settings, and process parameters to improve the lithography imaging performance. Among these methods, inverse lithography technology (ILT) is extensively used for mask optimization at advanced lithography technology nodes, owing to its unique advantages. ILT aims at improving lithography image fidelity through reverse calculation to optimize the main features (MF) and sub-resolution assist features (SRAF) on the mask patterns.

In the past, numerous research groups have proposed a variety of ILT algorithms, including the heuristic-based algorithms [4], parametric-based algorithms [5–7], and level-set-based (LSB) algorithms [8–10]. Heuristic-based ILT algorithms optimize the mask in a discrete space, which has the disadvantages of instability and slow computational speed. The parametric-based algorithms update the pixelated mask patterns using the gradient-based strategies, which can be implemented by the steepest gradient (SD) method [5], conjugate gradient (CG) method [6] and compressed sensing (CS) methods [6]. On the other hand, the LSB algorithms regard the mask as a continuum, and represent the mask pattern with an implicit function, which has strong topological continuity. LSB-ILT can somehow prevent the formation of small unwanted holes and extra openings during the mask optimization process, thus enhancing the mask manufacturability. Moreover, the LSB-ILT algorithms can improve the convergence speed, since they optimize the
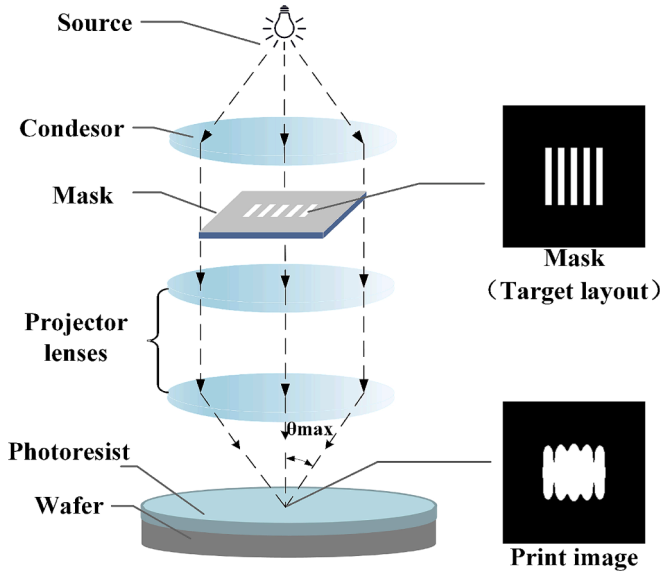
Fig. 1. The sketch of DUV optical lithography system.

mask topological shapes instead of mask pixels. In the past, some works discussed the formulations and modifications of the LSB-ILT methods [8–10]. Although machine learning and deep learning have shown the ability to improve the computational efficiency of ILT [11], the complex learning models inevitably induce longer training periods. Moreover, the requirements of large volume and high quality of training data present challenges for the real applications of ILTs.

In addition, the ILT algorithms may generate tiny and complex mask features that are difficult to fabricate. Although researchers have tried to reduce mask complexity by incorporating various regularization terms in the optimization cost function, those methods cannot strictly enforce the mask manufacturing constraints [5,6,12–14]. Subsequently, another variant of ILT, dubbed block-based ILT (BB-ILT), was proposed to iteratively optimize the mask under some critical manufacturability constraints [15].

This paper aims to optimize the mask as much as possible to improve the image fidelity and convergence speed, while satisfying some common manufacturing constraints. This study integrates the BB-ILT method with the level-set framework, where the mask pattern is represented by a set of basis blocks distributed on a level-set support region. Then, the level-set support region is updated by the gradient-based algorithm. It is noted that the traditional SD algorithm suffers from slow convergence rate and requires the selection of appropriate step size. Thus, by incorporating the Courant-Friedrichs-Lewy (CFL) condition [16], this paper employs the Barzilai-Borwein algorithm to adaptive modify the step size, thus accelerating the convergence process. In order to verify the proposed ILT method, a digital lithography testbed is established, employing the digital micromirror devices (DMD) to generate mask patterns, and using a charge coupled device (CCD) detector to capture the aerial images. A coherent imaging model with calibrated kernels is developed to simulate the image results of the digital lithography testbed. Then, we conduct simulations and real experiments to verify the proposed ILT method and compared it to the state-of-the-art methods.

The remainder of this paper is organized as follows. Section 2 introduces the lithography imaging model. Section 3 proposes the BB-LIT method based on level-set framework. Section 4 describes the BB-ILT solution based on the Barzilai-Borwein gradient method (BBGM). Section 5 reports the simulation findings at 45 nm technology node, proving the effectiveness of the proposed algorithm. Section 6 provides the real experimental results based on the digital lithography testbed. Section 7 summarizes the entire work.

2. Fundamental of the lithography imaging model

Given a mask pattern $M \in \mathbb{R}^{N \times N}$, according to the Abbe's theory of optical lithography, the aerial image $I \in \mathbb{R}^{N \times N}$ on wafer is formulated as [17]

$$I = \frac{1}{J_{sum}} \sum_{x_s} \sum_{y_s} \left(J(x_s, y_s) \times \sum_{p=x,y,z} \left(\left| H_p^{x_s y_s} \otimes (B^{x_s y_s} \odot M) \right|^2 \right) \right) \quad (1)$$

where (x_s, y_s) is the coordinate on the source plane; $J(x_s, y_s)$ is the intensity of the source point at (x_s, y_s); $J_{sum} = \sum_{x_s} \sum_{y_s} J(x_s, y_s)$ is a normalization factor; $H_p^{x_s y_s} \in \mathbb{R}^{N \times N}$ ($p = x, y, z$) is the point spread function (PSF) of lithography system along the p-axis; $B^{x_s y_s} \in \mathbb{R}^{N \times N}$ is the diffraction matrix of the mask; $\otimes$ is the convolution operation, and $\odot$ represents the Hadamard product. For simplicity, the hard threshold function $\Gamma\{\cdot\}$ is used to depict the development process of photoresist, and the print image $Z \in \mathbb{R}^{N \times N}$ on wafer is calculate as [5]

$$Z = \Gamma\{I, t_r\} \quad (2)$$

where t_r is a constant threshold of photoresist. To make the cost function differentiable, the sigmoid function is used to approximate hard threshold function [5]

$$Z \approx sig(I, a_r, t_r) = \frac{1}{1 + \exp[-a_r(I - t_r)]} \quad (3)$$

where a_r is the steepness index of the sigmoid function.

3. BB-ILT based on level-set framework

In order to improve the manufacturability, the block-based mask representation is adopted [15], where the mask pattern M is decomposed to a set of overlapped basis blocks as shown in Fig. 2, thus:

$$M = \Gamma(W_M \otimes \Theta_M - 1) + \Gamma(W_S \otimes \Theta_S - 1) \quad (4)$$

where $W_M \in \mathbb{R}^{N_M \times N_M}$ and $W_S \in \mathbb{R}^{N_S \times N_S}$ denote the binary basis blocks of the MFs and SRAFs, respectively (as shown in Fig. 2(a)); N_M and N_S represent the minimum lateral sizes of MFs and SRAFs, respectively; $\Theta_M \in \mathbb{R}^{N \times N}$ and $\Theta_S \in \mathbb{R}^{N \times N}$ are defined as the coefficient binary matrices of MFs and SRAFs, which represent the support areas (or locations) of the basis blocks (as shown in Fig. 2(b)). In the coefficient matrix shown as Fig. 2 (b), the white pixels with values of 1 represent the center positions of the basic blocks. The subsequent ILT process will restrict the distance between the MFs and SRAFs, and adjusts the sizes and positions of the basic blocks. This process can effectively reduce the isolated pixels in the mask pattern and improve the mask manufacturability.

Similar to Eq. (3), we use the sigmoid function to replace the hard threshold function in Eq. (4), then we have

$$M = sig(W_M \otimes \Theta_M, a_r, 1) + sig(W_S \otimes \Theta_S, a_r, 1). \quad (5)$$

Given the target layout $\widetilde{Z} \in \mathbb{R}^{N \times N}$ and the actual print image Z in Eq. (3), the BB-ILT problem can be formulated as following

$$(\widehat{\Theta}_M, \widehat{\Theta}_S) = \arg\min_{\Theta_M, \Theta_S} F \quad (6)$$

where $\widehat{\Theta}_M$ and $\widehat{\Theta}_S$ are the optimal coefficient matrices; $F = \left\| \sqrt{\Pi} \left(Z - \widetilde{Z} \right) \right\|_2^2$ is the cost function representing the pattern error (PE), and $\Pi \in \mathbb{R}^{N \times N}$ is a weight matrix to modulate the cost values in different regions.

We use level set functions (LSFs) ϕ_M and ϕ_S to describe the coefficient matrices Θ_M and Θ_S, respectively. The commonly used LSF is the signed distance function [16], namely

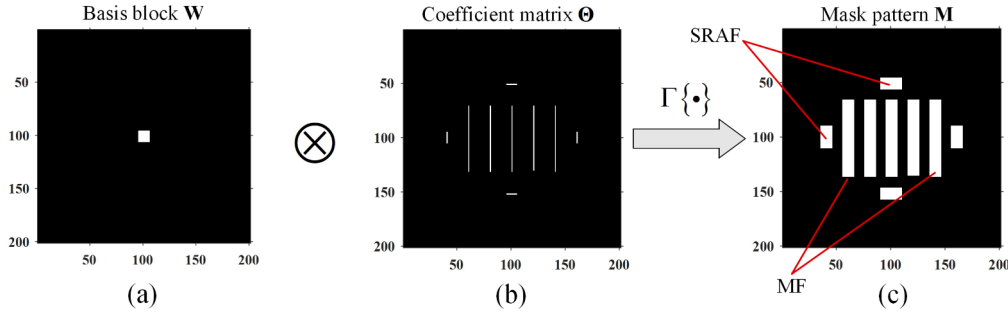Fig. 2. Mask formation process based on the basis block.

$$\phi_M(\boldsymbol{r}) = \begin{cases} -d_M(\boldsymbol{r}) & \boldsymbol{r} \in \partial\boldsymbol{\Theta}_M^- \\ 0 & \boldsymbol{r} \in \partial\boldsymbol{\Theta}_M \\ d_M(\boldsymbol{r}) & \boldsymbol{r} \in \partial\boldsymbol{\Theta}_M^+ \end{cases} \phi_S(\boldsymbol{r}) = \begin{cases} -d_S(\boldsymbol{r}) & \boldsymbol{r} \in \partial\boldsymbol{\Theta}_S^- \\ 0 & \boldsymbol{r} \in \partial\boldsymbol{\Theta}_S \\ d_S(\boldsymbol{r}) & \boldsymbol{r} \in \partial\boldsymbol{\Theta}_S^+ \end{cases} \quad (7)$$

where $\boldsymbol{r}$ represents the spatial coordinate (x, y); $\partial\boldsymbol{\Theta}_M$ and $\partial\boldsymbol{\Theta}_S$ respectively denote the boundaries of $\boldsymbol{\Theta}_M$ and $\boldsymbol{\Theta}_S$; $\partial\boldsymbol{\Theta}^-$ and $\partial\boldsymbol{\Theta}^+$ represent the inner and outer regions of the coefficient matrix; $d(\boldsymbol{r})$ is the minimum Euclidean distance from the location (x, y) to the boundaries. Therefore, the coefficient matrices can be represented by LSF as

$$\boldsymbol{\Theta}_M(\boldsymbol{r}) = \begin{cases} 1 & \text{if } \phi_M(\boldsymbol{r}) \leqslant 0 \\ 0 & \text{if } \phi_M(\boldsymbol{r}) > 0 \end{cases} \boldsymbol{\Theta}_S(\boldsymbol{r}) = \begin{cases} 1 & \text{if } \phi_S(\boldsymbol{r}) \leqslant 0 \\ 0 & \text{if } \phi_S(\boldsymbol{r}) > 0 \end{cases} \quad (8)$$

It is worth noting that in the proposed method, the optimization target is the coefficient matrix, which encodes the position information of the basis blocks. Given the property of level set function, the coefficient matrix is binarized after every iteration based on sign distinctions, facilitating the mask computation. Thus, the coefficient matrix within the proposed ILT framework is a binary matrix. According to Eqs. (7) and (8), Eq. (6) can be modified as $(\widehat{\phi}_M, \widehat{\phi}_S) = \text{argmin}_{\phi_M, \phi_S} F$. Then, we can derive the evolution equations of the LSFs as follow [17]

$$\frac{\partial\phi_M}{\partial t} = -v_M(\boldsymbol{r}, t) \cdot |\nabla\phi_M| \frac{\partial\phi_S}{\partial t} = -v_S(\boldsymbol{r}, t) \cdot |\nabla\phi_S| \quad (9)$$

where $v_M(\boldsymbol{r}, t)$ and $v_S(\boldsymbol{r}, t)$ are the evolution velocities.

4. LBB-ILT solution based on BBGM

This section introduces the BBGM to solve the BB-ILT problem in Section 3, which utilizes adaptive step size to improve the convergence speed. The BBGM can overcome the shortcomings of the SD algorithm by updating the step size appropriately [18]. The workflow of the proposed BB-ILT algorithm is outlined in Fig. 3. To reduce the convergence error, we optimize the MFs and SRAFs simultaneously, while enforcing the minimum space between them to be larger than a predefined threshold ε_D [15]. Additionally, other manufacturing constraints are adopted [15]. Firstly, the minimum lateral sizes of MFs and SRAFs must be larger than the predefined thresholds ε_M and ε_S, respectively. Secondly, the mask should not contain the 'risky jogs' defined as the unmanufacturable edge protrusions. According to [15], the height of risky jog is less than a predefined small threshold (height threshold), and at least one of its adjacent lengths is shorter than another pre-defined threshold (arm threshold). In the mask optimization process, the algorithm will check

all the concave corners in the mask pattern and find out the risky jogs. Subsequently, the risky jogs are smoothed by filling operation or cutting operation. This procedure is performed many times until all the risky jogs are repaired [15].

In **Step** 1, we initialize the LSFs $\phi_M(\boldsymbol{r}, t_0)$ and $\phi_S(\boldsymbol{r}, t_0)$ according to the initial MF pattern $\boldsymbol{M}_{\text{main}}^0$, initial SARF pattern $\boldsymbol{M}_{\text{SRAF}}^0$ and Eq. (7). In **Step** 2, we update the LSF and the coefficient matrix of MF. Firstly, we calculate the evolution velocity $v_M(\boldsymbol{r}, t_k)$ of MF in the kth iteration. Equation (9) is a partial differential equation. In order to guarantee the convergence and stability of the solution, we can define the time step via the CFL condition as

$$\Delta t_{M,k} \cdot \max\left\{\frac{|v_M(\boldsymbol{r}, t_k)|}{h}\right\} = \alpha_M \quad (10)$$

where h is the grid size of the discrete Cartesian, and $\alpha_M \in (0, 1)$ is the CFL number. However, the time step derived from the CFL condition is known to decelerate the convergence rate [19]. To address this issue, the present study adopts an improved Barzilai-Borwein time step strategy, which seeks to increase the time step to improve convergence efficiency. In particular, when $k = 1$, we set the initial time step $\Delta t_{M,1}$ according to Eq. (10); when $k \geqslant 2$, we can calculate the Barzilai-Borwein time step as [20,21]

$$\Delta t_{M,k}^{NBB} = \frac{\|S_{M,k-1}\|_2^2}{\|Y_{M,k-1}\|_2^2} \quad (11)$$

where $S_{M,k-1} = \phi_M(\boldsymbol{r}, t_k) - \phi_M(\boldsymbol{r}, t_{k-1})$ and $Y_{M,k-1} = v_M(\boldsymbol{r}, t_k) - v_M(\boldsymbol{r}, t_{k-1})$. Therefore, the time step of the MF in the kth iteration can be expressed as

$$\Delta t_{M,k}^{BB} = \begin{cases} \Delta t_{M,k}^{NBB} & \text{if } \Delta t_{M,k} \leqslant \Delta t_{M,k}^{NBB} \leqslant 10\Delta t_{M,k} \text{ and } k \geqslant 2 \\ 10 * \Delta t_{M,k} & \text{if } 10\Delta t_{M,k} \leqslant \Delta t_{M,k}^{NBB} \text{ and } k \geqslant 2 \\ \Delta t_{M,k} & \text{otherwise} \end{cases} \quad (12)$$

As shown in Eq. (12), the CFL condition is involved to limit the Barzilai-Borwein time step to prevent convergence oscillation caused by excessively large time step. It is noted that Eq. (9) is a partial differential equation, which is discretized to find the optimal LSF. Therefore, in the $k + 1$th iteration, we will update the LSF as following:

$$\phi_M(\boldsymbol{r}, t_{k+1}) = \phi_M(\boldsymbol{r}, t_k) - v_M(\boldsymbol{r}, t_k) \cdot \Delta t_{M,k}^{BB} \quad (13)$$

where $\Delta t_{M,k}^{BB}$ is calculated by Eq. (12). Finally, we can update the $\boldsymbol{\Theta}_M^{k+1}$
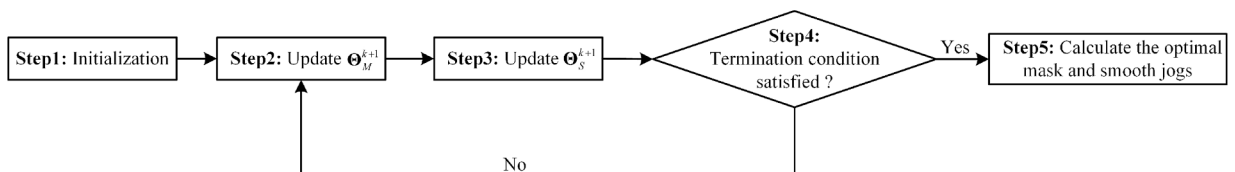

Fig. 3. The flowchart of the BB-ILT algorithm.

and $\boldsymbol{M}^k$ according to Eq. (8) and Eq. (5), respectively.

As shown in Fig. 3, we will update the LSF and coefficient matrix of SRAF in **Step** 3. The process of optimizing Θ_S^{k+1} is similar to **Step** 2. For the SRAF, we calculate the time step $\Delta t_{S,k}^{BB}$ and update $\phi_S(\boldsymbol{r}, t_{k+1})$ as

$$\phi_S(\boldsymbol{r}, t_{k+1}) = \phi_S(\boldsymbol{r}, t_k) - v_S(\boldsymbol{r}, t_k) \cdot \Delta t_{S,k}^{BB} \tag{14}$$

Finally, we can update the Θ_S^{k+1} and limit the distance between MF and SRAF.

In **Step** 4, we need to evaluate if the termination criteria are satisfied. In general, the termination criteria are defined either achieving the predetermined maximum iteration number or reducing the PE to an acceptable level. Upon satisfying the termination conditions, the workflow skips to **Step** 5, where the optimal binary mask pattern $\widehat{\boldsymbol{M}}_b$ is calculated based on Eq. (4), and the unmanufacturable jogs will be smoothed using the methods described in [15]. Otherwise, the algorithm returns **Step** 2 and continue the loop.

5. Simulation and analysis

This section provides the simulation results of the proposed method based on different layout patterns at the advanced technology node of integration circuits. Here, we compare the proposed BB-ILT using level-set framework (LBB-ILT) with the traditional LSB-ILT (refer to [17]), pixelated-ILT (refer to [6]) and traditional BB-ILT (refer to [15]) in terms of PE, edge placement error (EPE), convergence speed, and mask manufacturability.

In this paper, EPE is defined as the average offset dimension between the resist image contour and the target contour at all pixels along the boundary of target layout, where the EPE measurement points are uniformly selected across all edges. The EPE can be calculated as $\text{EPE} = \oint_c \text{EPE}_c dc / L_c$ [22]. In this equation, EPE_c represents the offset dimension between the resist image contour and the target contour at a certain point on the boundary of target layout; $\oint_c \cdot dc$ represents the line integral along the boundary; L_c is the perimeter of target layout boundary. A smaller EPE value indicates the higher fidelity of resist image.

In this paper, we use the number of trapezoids fractured from the mask pattern as the criterion to assess the mask manufacturability. The fewer trapezoid count means the lower mask complexity and better manufacturability [23]. Furthermore, in this study, to assess the robustness of the lithographic process, we have considered the effects of defocus δ and exposure dose variations η on the imaging performance. All of the computations are performed on an Intel (R) Core (TM) i7-12700 CPU, 4.9 GHz, and 32 GB of RAM.

Fig. 4(a) presents a target layout of line-space geometries with 45 nm CD and 1:1 duty ratio. The overall area of the mask is 4020 nm × 4020
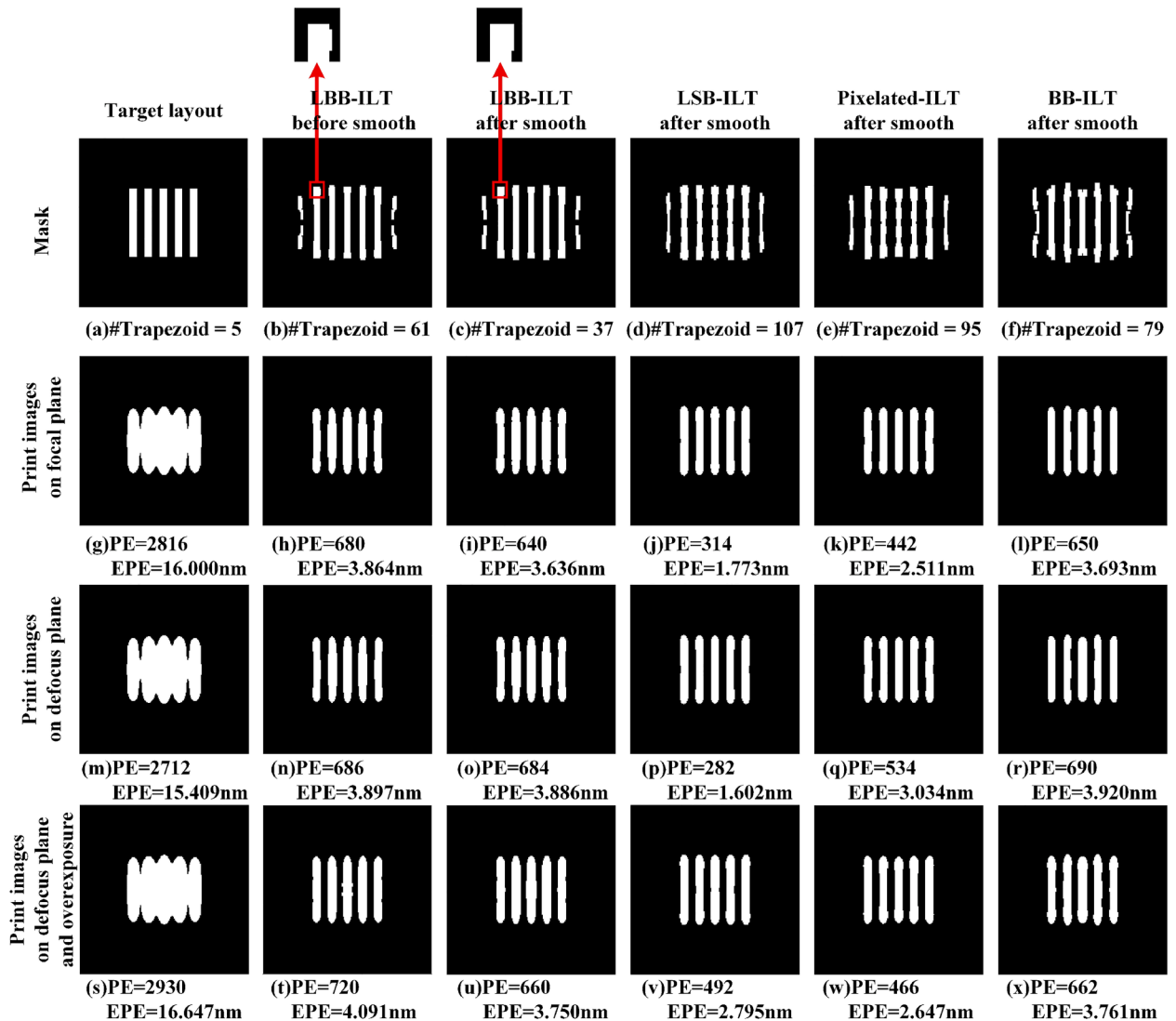

Fig. 4. Simulations of LBB-ILT, LSB-ILT, pixelated-ILT and BB-ILT based on line-space pattern with 45 nm CD.

nm. The light source of lithography system uses an annular illumination with 193 nm wavelength, where the inner and outer partial coherence factors are $\sigma_{\text{inner}} = 0.82$ and $\sigma_{\text{outer}} = 0.97$, respectively. An immersion lithography system with numerical aperture (NA) of 1.2 is used. In Eq. (3), we set $t_r = 0.2$ and $a_r = 25$. In Eq. (4), we set $N_M = 5$ and $N_S = 3$ to constrain the minimum lateral sizes of MFs and SRAFs. Besides, the allowable distance between MF and SRAF should be larger than 240nm. In Eq. (6), we set $\Pi(m, n) = 1.6$ in the region extending 5 pixels outward from the target boundary, while we set $\Pi(m, n) = 1$ in other areas. Besides, we set defocus $\delta = 40$ nm and exposure dose variations $\eta = 1.05$ to show the robustness of the lithographic process.

Fig. 4 compares the simulation results of the proposed LBB-ILT method with the traditional LSB-ILT, pixelated-ILT and BB-ILT method. All methods employ the CG algorithm to update the optimization variables. For the LBB-ILT, we set CFL numbers of MFs and SRAFs to 0.5 and 0.3, with 100 iterations in total, respectively, while the CFL number of the LSB-ILT is set as 0.5. For the traditional BB-ILT, the step sizes for optimizing the MFs and SRAFs are set as 22, with 200 iterations in total, while the step size of pixelated-ILT is set as 15. From top to bottom, Fig. 4 shows the mask patterns, the print images on the focal plane, the print images on the defocus plane with $\delta = 40$ nm with normal exposure dose, and the print images on the defocus plane with $\delta = 40$ nm with 5 % overexposure dose. The first column shows the simulation results of the initial mask pattern, while the second and the third columns present the mask patterns optimized by the LBB-ILT before and after jog smoothing, respectively, along with their print images. The fourth, the fifth and the sixth columns illustrate the mask pattern optimized by the traditional LSB-ILT, pixelated-ILT and BB-ILT methods after jog smoothing and their corresponding print image, respectively. A small mask region is magnified to illustrate the effectiveness of the jog smoothing operation. It shows that the jog smoothing step not only preserves the image fidelity, but also improves the mask manufacturability. Specifically, compared to the initial case, the LBB-ILT achieves 76 % reduction of PE, in contrast to the 89 % and 84 % reductions of PEs achieved by the LSB-ILT and pixelated-ILT, respectively. At the same time, the EPEs generated by different ILT methods as shown in Fig. 4 have decreased significantly compared to the initial layout. But, the LBB-ILT results in much fewer trapezoid count compared to the LSB-ILT and pixelated-ILT. That is because the LBB-ILT uses the basis blocks to represent mask pattern, thus can effectively improve the manufacturability. Additionally, the results demonstrate that our proposed algorithm maintains considerable robustness different process conditions.

Different from the proposed LBB-ILT, traditional BB-ILT described in [15] directly optimizes the coefficient matrices in pixel level, instead of optimizing the level-set support regions. Comparing the results of LBB-ILT and BB-ILT methods in Fig. 4, it is observed that the final PE values obtained by both methods are similar to each other. However, the trapezoid count obtained by LBB-ILT is significantly smaller than that of traditional BB-ILT. Furthermore, the LBB-ILT shows much faster and smoother convergence than the BB-ILT in Fig. 5(a), where the

convergence curves of BB-ILT and LBB-ILT based on the CG method are respectively shown as black solid curve and blue dash-dotted curve. The benefits of LBB-ILT are likely due to the level-set framework that optimizes the support regions of coefficient matrices thus ensuring the continuity of the mask pattern. In the BB-ILT, each iteration involves updating the pixels of the coefficient matrix, which can occasionally result in isolated pixels undergoing abrupt changes. Given that each pixel in the coefficient matrix represents the position of a substantial basic block, such abrupt change of the coefficient matrix will significantly change the mask pattern, which may lead to some oscillations in the convergence process. Conversely, the proposed LBB-ILT method employs a level set function to delineate the boundaries of coefficient matrix. During each iteration, this function evolves, resembling the expansion or contraction of the contours. This evolution process tends to prevent sudden changes or isolated pixels of the coefficient matrix, thereby ensuring the continuity of mask shape. Thus, the proposed method is beneficial to achieve faster and more stable convergence.

Next, we prove the advantage of BBGM used in the proposed method based on an ablation experiment. Fig. 5(a) shows the PE convergence curves of LBB-ILT methods using the BBGM and CG algorithm represented by the green dotted line and the blue dash-dotted line to update optimization variables, respectively. It shows that the BBGM reduces the PE to 650 after 39 iterations, whereas the CG algorithm requires 71 iterations. As depicted in Fig. 5(a), using BBGM can effectively accelerate the convergence compared to the CG algorithm. This is because the step size of CG algorithm is constrained by the CFL condition, limiting the convergence rate. In contrast, the BBGM determines the optimal step size based on the secant equation, thereby improving the convergence rate.

The universality of the proposed method is further investigated based on the simulations of complex layout with 45 nm CD, as shown in Fig. 6(a). In this simulation, the light source uses the TE-polarization, with the remaining system parameters consistent with those described previously. In Fig. 6, the first column shows the simulation results for the target layout, while the second to the fifth columns respectively display the results of the proposed LBB-ILT, LSB-ILT, pixelated-ILT and BB-ILT after jog smoothing. Compared to the initial case, the LBB-ILT reduces the PE by 77.1 %, while the LSB-ILT and pixelated-ILT achieves 83.9 % and 82.0 % reductions of PEs, respectively. The LBB-ILT method can also reduce the EPE effectively compared to the initial layout. However, the LBB-ILT can significantly enhance the mask manufacturability without substantially impacting lithography imaging performance. In addition, the LBB-ILT has lower mask complexity than the BB-ILT. Moreover, the convergence curves of BBGM and CG algorithms are represented by the green dotted line and the blue dash-dotted line in Fig. 5(b), respectively, which demonstrate the benefit of BBGM in improving the convergence speed.

The generalization capability and effectiveness of the proposed methods are further verified through the simulations using the layout selected from the ICCAD-2013 contest dataset [24], as illustrated in
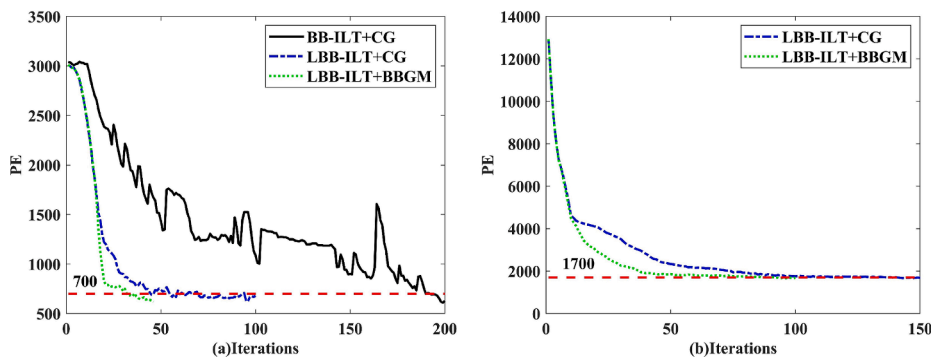

Fig. 5. Convergence curves of LBB-ILT based on different optimization algorithms and traditional BB-ILT using (a) the line-space layout, and (b) the complex layout.
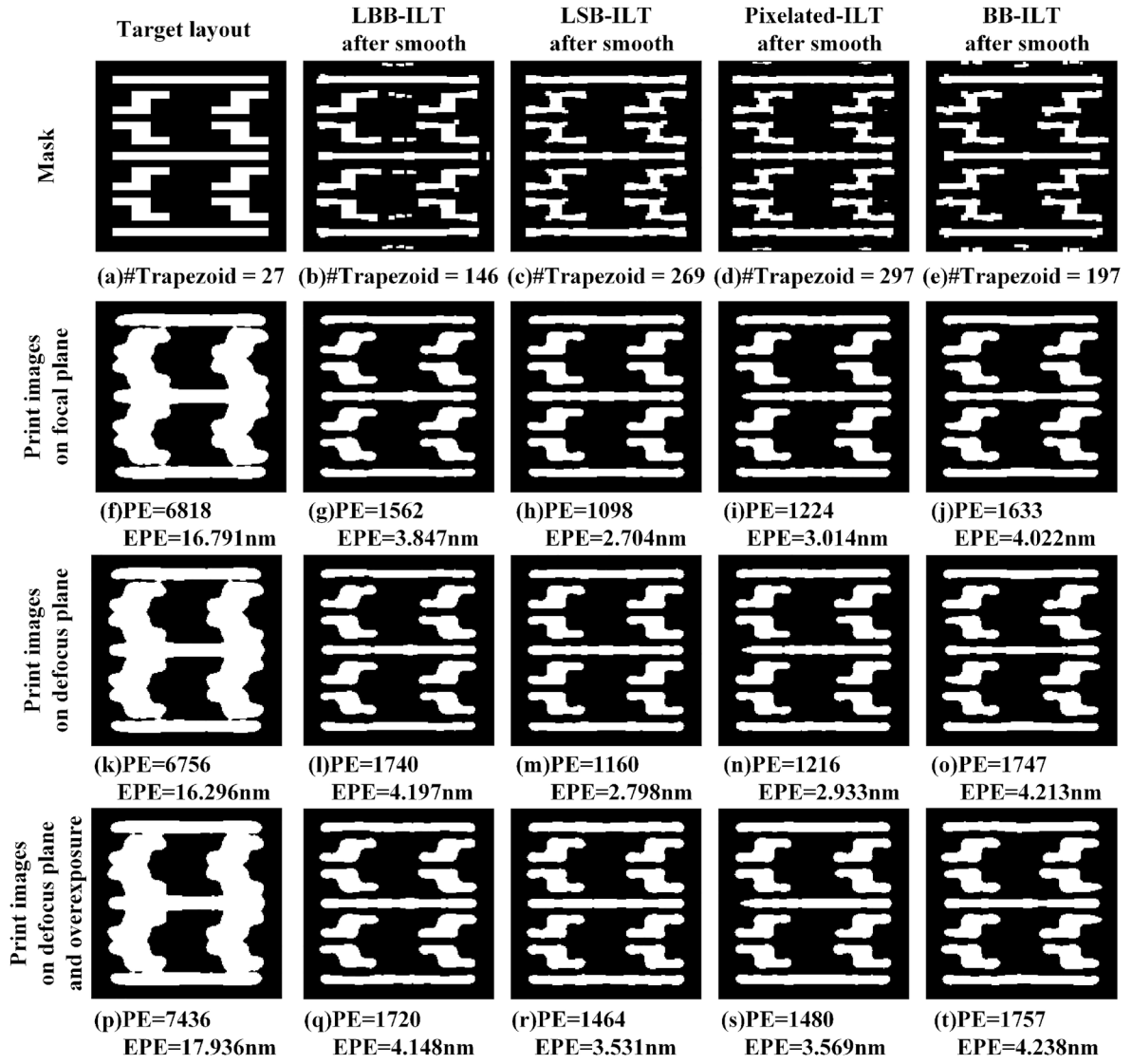
	Target layout	LBB-ILT after smooth	LSB-ILT after smooth	Pixelated-ILT after smooth	BB-ILT after smooth
Mask	(a)#Trapezoid = 27	(b)#Trapezoid = 146	(c)#Trapezoid = 269	(d)#Trapezoid = 297	(e)#Trapezoid = 197
Print images on focal plane	(f)PE=6818 EPE=16.791nm	(g)PE=1562 EPE=3.847nm	(h)PE=1098 EPE=2.704nm	(i)PE=1224 EPE=3.014nm	(j)PE=1633 EPE=4.022nm
Print images on defocus plane	(k)PE=6756 EPE=16.296nm	(l)PE=1740 EPE=4.197nm	(m)PE=1160 EPE=2.798nm	(n)PE=1216 EPE=2.933nm	(o)PE=1747 EPE=4.213nm
Print images on defocus plane and overexposure	(p)PE=7436 EPE=17.936nm	(q)PE=1720 EPE=4.148nm	(r)PE=1464 EPE=3.531nm	(s)PE=1480 EPE=3.569nm	(t)PE=1757 EPE=4.238nm

Fig. 6. Simulations of LBB-ILT, LSB-ILT, pixelated-ILT and BB-ILT based on complex layout with 45 nm CD.

Fig. 7(a). In this simulation, a TE-polarized light source is employed, while all other system parameters remain consistent with the previously described setup. In Fig. 7, the first column presents the simulation results for the target layout, while the second to the fifth columns display the results for the methods of LBB-ILT, LSB-ILT, pixelated-ILT, and BB-ILT after jog smoothing, respectively. Compared to the initial case, the proposed LBB-ILT method reduces the PE by 77.4 %, with the LSB-ILT and pixelated-ILT achieving the reductions of 82.0 % and 80.7 %, respectively. Furthermore, the LBB-ILT can achieve significant improvement in mask manufacturability without adversely affecting the lithography imaging performance. Additionally, it offers reduced mask complexity and better substantial robustness compared to the BB-ILT.

It is worth noting that the traditional ILT methods tend to generate curvilinear masks. However, our proposed method aims at solving the manufacturing challenge of the curvilinear mask patterns obtained by ILT approaches. In the proposed method, the mask pattern is composed of a set of basis blocks. The positions of the basis blocks are determined by the coefficient matrix, where each pixel in the coefficient matrix can be optimized individually, and thus the position of basis block can be adjusted at the pixel-wise step. Thus, the optimized mask pattern obtained by the proposed method is more regular and manufacture-friendly compared to the traditional ILT method. In addition, the degrees of optimization freedom are also maintained by the pixel-based

coefficient matrix.

6. Experiment based on digital lithography testbed

In this section, we use the experimental results obtained on the digital lithography testbed to validate the proposed method. Section 6.1 briefly describes the digital lithography testbed built in our lab. Section 6.2 describes the calibration method of the imaging model for the real system. Section 6.3 provides the experimental results of the test layouts, where the proposed method is compared with the state-of-the-art ILT method.

6.1. The digital lithography testbed

In this paper, we establish a DMD maskless lithography testbed to conduct the principle experiment and to verify the proposed methods. This kind of principle experiments were used to verify some advanced computational lithography algorithms in the previous research works. It is noted that our experiment testbed is different from the real DUV or EUV lithography systems. The DUV lithography system uses the Kohler illumination system and a set of high-precision projection lenses. On the other hand, the EUV lithography system adopts the illumination with 13.5 nm wavelength, and uses the fully-reflective optical architecture
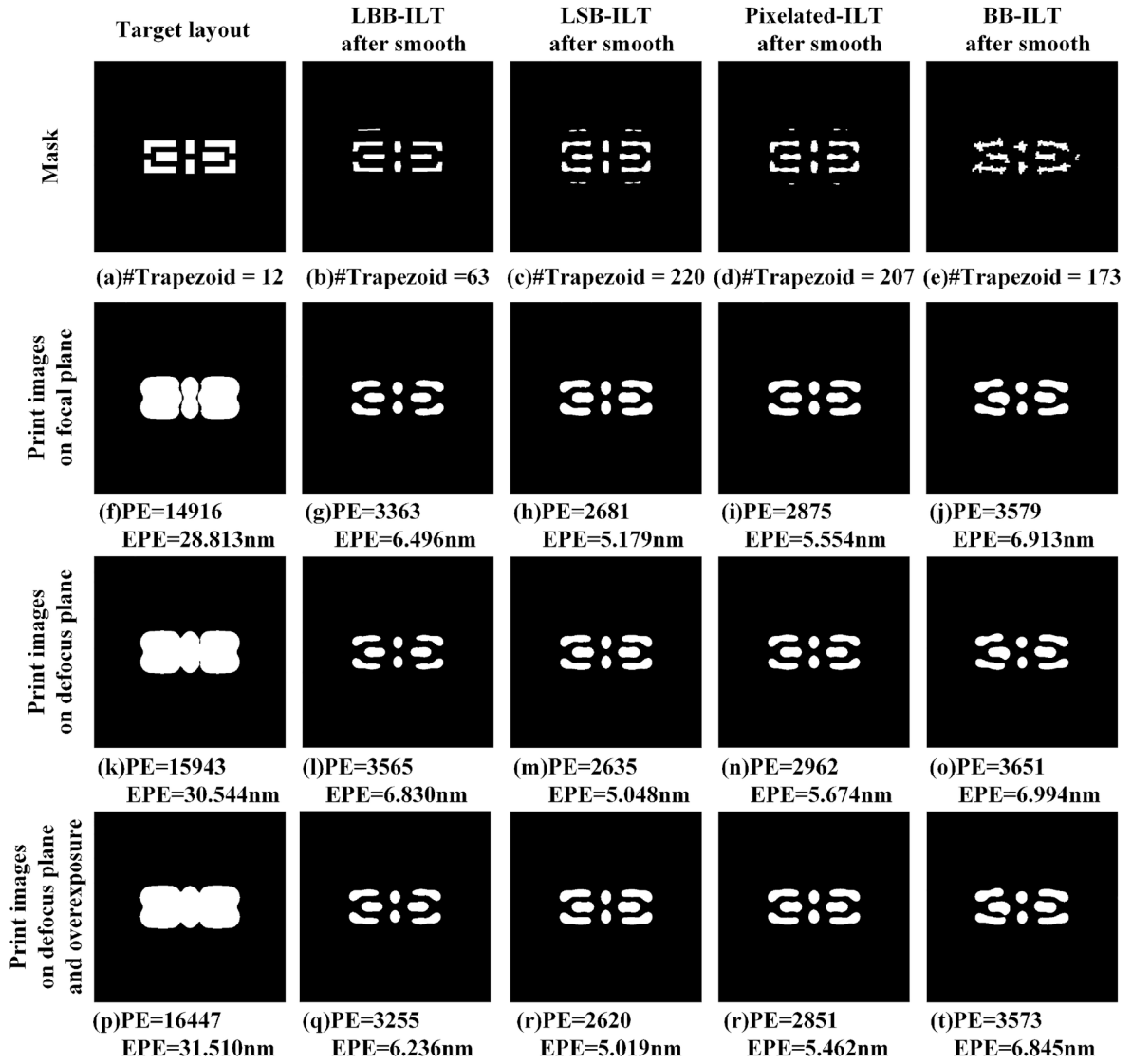
Fig. 7. Simulations of LBB-ILT, LSB-ILT, pixelated-ILT and BB-ILT based on the layout selected from the ICCAD-2013 contest dataset.

including the reflective mask and reflective lens group to transmit the light wave onto the wafer. In addition, in the real lithography process, the effects of photoresist exposure and development, and the process variations like defocus and dose variation should also be considered. I the future work, we will involve those non-ideal factors in the proposed ILT algorithms, and we will try to upgrade our digital lithography testbed to involve more professional optical design and system structure.

Fig. 8 presents the schematic illustration and the picture of the digital lithography testbed established by our group [25–27]. A light emitting diode (LED) is used as the light source, whose central wavelength is $\lambda = 620$ nm and the lower and upper limits of the spectrum are $\lambda_1 = 580$ nm and $\lambda_2 = 642$ nm, respectively. A plano-convex lens with 50 mm focal length is used for light beam collimation. A pair of fly's eye lenses alongside a condenser lens are used for light wave homogenization. This
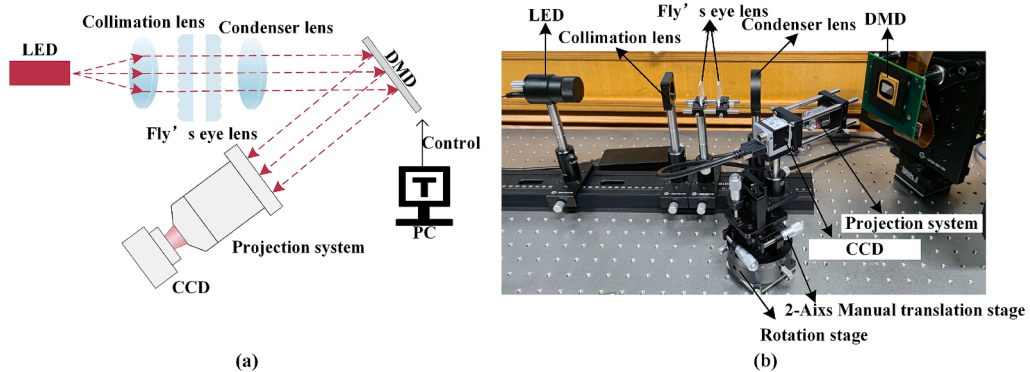

Fig. 8. The digital lithography testbed used to verify the proposed method: (a) the schematic illustration and (b) the picture of the digital lithography testbed.

arrangement ensures a consistent and uniform projection on the DMD that hosts 1920 × 1080 micromirror array with 10.8 μm micromirror pitch. The DMD allows the freeform modulation of light intensity to create a virtual mask. A microscope objective with 0.1NA is utilized to gather the reflected light rays from DMD, and to project them on a CCD detector. The detector can be finely adjusted using a rotation stage and a translation stage to determine the focus of the print pattern. By carefully adjusting the object plane and image plane, a direct correspondence between the micromirror element and the CCD element is achieved. What is captured by the CCD detector is the aerial image, which can be regarded as a grey-scale image. Due to limitation of experimental conditions, the photoresist effect is simulated by a mathematical model as described in Section 2.

6.2. Calibration of imaging model for the digital lithography testbed

Considering the low-NA of the projection optics and the spectral bandwidth of the light source, the aerial image generated by the testbed can be formulated as [28]

$$I^\lambda = \frac{1}{J_{sum}} \sum_{x_s} \sum_{y_s} \left(J(x_s, y_s) \times \left| H^{x_s, y_s, \lambda} \otimes M \right|^2 \right) \tag{15}$$

where $H^{x_s, y_s, \lambda}$ is the PSF corresponding to the wavelength λ. Since the LED is a quasi-monochromatic light source, the formulation of aerial image can be adjusted as follows

$$I = \frac{1}{C_{sum}} \sum_{\lambda=\lambda_1}^{\lambda_2} C(\lambda) \cdot I^\lambda \tag{16}$$

where $C(\lambda)$ represents the spectrum of light source within the range between λ_1 and λ_2; C_{sum} is a factor to normalize the energy of aerial image.

Additionally, an extra convolution kernel G is introduced to simulate the influence of non-ideal factors of the testbed [29]. These factors may include optical aberrations, flare, system assembly error, and pixel mismatch between DMD and detector. Thus, the aerial image can be calculated as

$$I_C = G \otimes I \tag{17}$$

In the testbed, the LED light source with a pinhole is approximated as a point source, which simplifies Eq. (15) by reducing the equation to a single source point at $x_s = y_s = 0$. Consequently, Eq. (17) is rewritten as follows

$$I_C = G \otimes \frac{1}{C_{sum}} \sum_{\lambda=\lambda_1}^{\lambda_2} C(\lambda) \cdot \left| H^{x_s, y_s, \lambda} \otimes M \right|^2 \tag{18}$$

In order to improve the simulation accuracy, we need to calibrate the

imaging model by fitting optimizing the kernels G and $H^{x_s, y_s, \lambda}$ to fit a group of training layouts. Fig. 9(a) and 9(b) illustrate the training layouts and simple testing layouts used in this paper, all of which have the dimension of 56 × 56. And Fig. 9(c) shows the complex testing layout with the dimension of 200 × 200. This goal of the model calibration process is to align the simulated aerial images to the real images captured by the CCD detectors. Given the simulated aerial images or the experimental aerial images, the print images can be calculated by using the photoresist model in Eqs. (2) and (3) with the parameters of $a_r = 25$ and $t_r = 0.1$. In particular, due to the defocus phenomenon caused by different fields of view, for complex mask layouts, the errors in different sub-regions are different. Therefore, it is very necessary to calibrate each sub-region and then stitch their aerial images up together. The specific calibration process for complex mask pattern can be found in Ref. [27].

6.3. Experimental results based on the testbed

In this subsection, we first use the numerical algorithms mentioned above to obtain the optimized ILT masks of the testing layouts in Fig. 9 (b). Then, we upload the data to the DMD to generate virtual masks, and capture the real aerial images and print images using the testbed. The superiority of the proposed methods will be substantiated based on the experimental results. Due to the relatively large pixel size of the DMD, the separate SRAFs on the virtual mask will easily generate extra-printing on the focal plane of CCD detector [30]. Thus, we exclude the SRAFs in the ILT algorithms and only optimize the MFs on the virtual mask. Regarding parameters, we set $t_r = 0.1$, $a_r = 25$ in Eq. (3), $N_W = 3$ and $N_S = 0$ in Eq. (4), and proceed with the algorithms for 50 iterations. Initially, we compare the optimization results obtained by the LBB-ILT methods with BBGM and CG algorithms based on one testing layout, and their convergence curve are shown in Fig. 9(d), where the blue dash-dotted line and the green dashed line correspond to the CG and BBGM algorithms, respectively. It was observed that for simple mask layout, using the BBGM and CG algorithms to update the variables will lead to similar performance. Nevertheless, the digital lithography testbed has the virtual mask with big size and non-significant diffraction effects, which contribute to minor initial errors and resulting in more serious fluctuations in convergence curves. In order to improve the convergence stability, an approach is adopted where only 10 % of the optimization variables with most significant gradient values are updated in subsequent iteration, while keeping other optimization variables unchanged. The resulting convergence curve is shown by the red solid curve in Fig. 9 (d). It shows that this strategy, referred to as "BBGM + select10%", leads to very smooth convergence curve without oscillation after 27 iterations. Thus, we apply this optimization strategy consistently in all subsequent experiments.

Fig. 10(a), 10(b) and 10(c) illustrate the experimental results for all of the three simple testing layouts in Fig. 9(b). From top to bottom, each
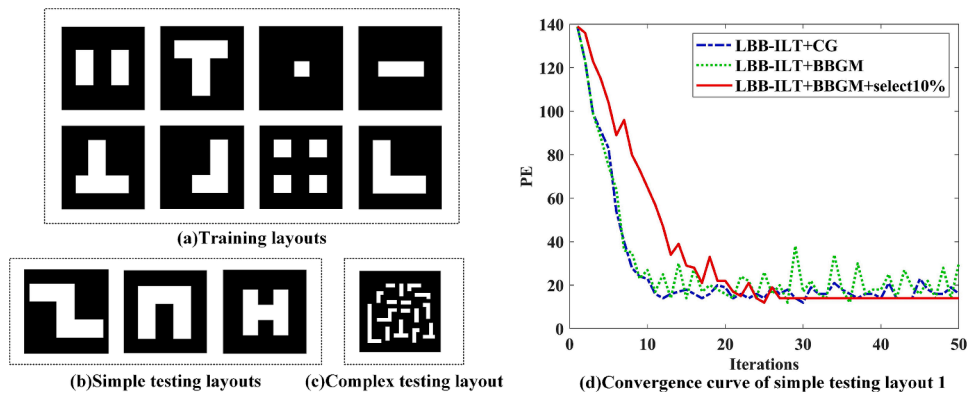

(a)Training layouts

(b)Simple testing layouts　　(c)Complex testing layout

(d)Convergence curve of simple testing layout 1

Fig. 9. The layout patterns used in the experiments and the convergence curves of different ILT methods: (a) the training layouts, (b) the simple testing layouts, (c) the complex testing layout, and (d) the convergence curves of the simple testing layout 1.
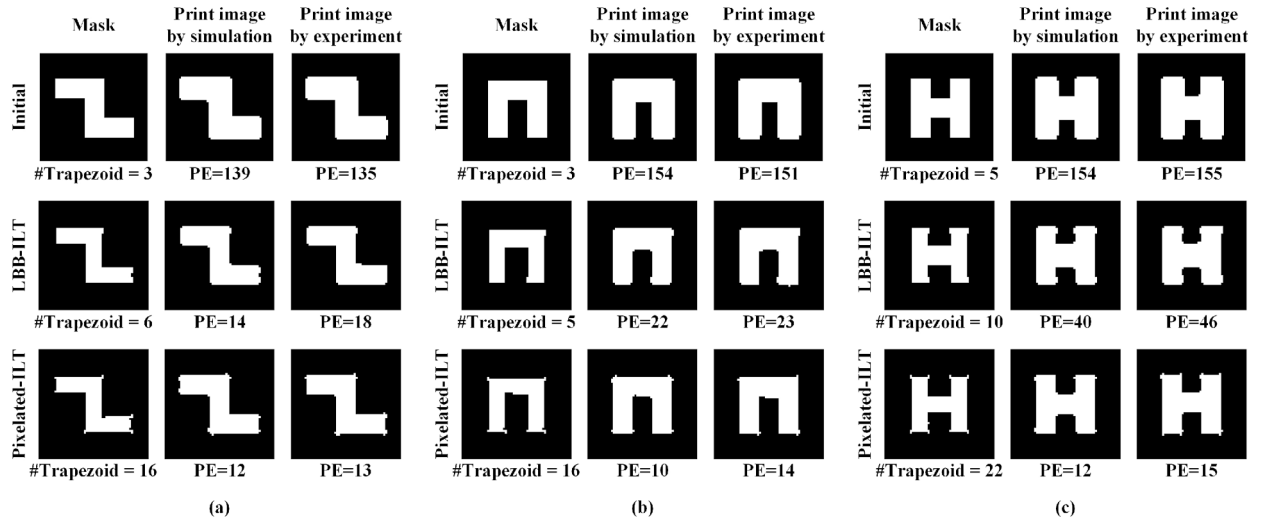
Fig. 10. Experimental results of the LBB-ILT and pixelated-ILT methods after jog smoothing based on three simple testing layouts.

subfigure shows the results of the target patterns before optimization, the results of the proposed LBB-ILT method, and the results of the traditional pixelated-ILT method after jog smoothing. In each subfigure, the first column shows the mask patterns, the second column shows the corresponding print images calculated by simulation models, and the third column shows the print images captured from the digital lithography testbed. The PE values of all print images and the trapezoid numbers of all mask patterns are presented. It is observed that the simulated and experimental print images have similar PE values, which substantiates the accuracy of the calibrated imaging model in characterizing the imaging process of the digital lithography testbed. Analogous to the simulation findings in Section 5, the pixelated-ILT method after jog smoothing surpasses the LBB-ILT in image fidelity on the testbed, but the mask complexity is higher than the LBB-ILT.
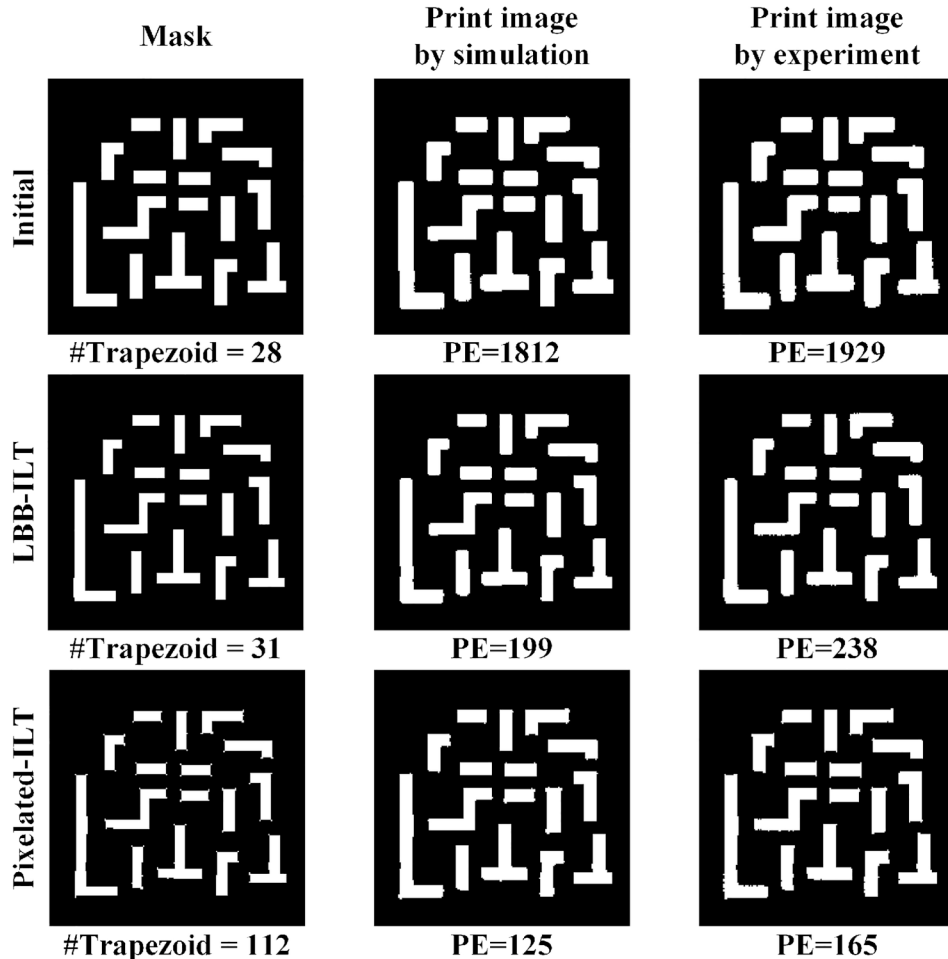

Fig. 11. Experimental results of the LBB-ILT and pixelated-ILT methods after jog smoothing based on the complex testing layout.

Fig. 11 illustrates the experimental results of the LBB-ILT and pixelated-ILT methods based on complex testing layout in Fig. 9(c). From this experiment, we can obtain the similar conclusion as that of Fig. 10. All of the experiments demonstrate the effectiveness and universality of the proposed LBB-ILT method.

7. Conclusion

This research developed a novel computational lithography method, dubbed LBB-ILT for effectively enhancing the lithography image fidelity and mask manufacturability. In this context, BBGM was combined with conventional CFL constants to improve the convergence efficiency and stability of the algorithm. For the advanced technology node, the proposed LBB-ILT method was compared with the traditional LSB-ILT, pixelated-ILT and BB-ILT, in aspects such as imaging performance, process robustness, convergence speed and mask manufacturability. Furthermore, the simulation outcomes indicated that the BBGM method was capable of further accelerating the convergence rate. A DMD-based lithography testbed was constructed to verify the proposed method. Through a comprehensive set of simulations and experiments, the superiority and universality of the proposed methods were proved, demonstrating the applicability of the proposed methods across various layout patterns.

Funding

CRediT authorship contribution statement

Chaojun Huang: Writing – original draft, Validation, Software, Methodology, Investigation. **Xu Ma:** Writing – review & editing, Project administration, Methodology, Investigation, Conceptualization. **Shengen Zhang:** Writing – review & editing, Investigation. **Mu Lin:** Writing – review & editing, Data curation. **Néstor Porras-Díaz:** Writing – review & editing, Supervision, Data curation. **Gonzalo R. Arce:** Supervision, Investigation, Conceptualization.

Declaration of competing interest

The authors declare that they have no known competing financial interests or personal relationships that could have appeared to influence the work reported in this paper.

Data availability

The data that has been used is confidential.

References

[1] F. Schellenberg, A little light magic, IEEE Spectr. 40 (9) (2003) 34–39.

[2] X. Ma, G.R. Arce, Computational Lithography, 1st ed., John Wiley and Sons, 2010.

[3] S. Zheng, B. Yu, M. Wong, OpenILT: an open source inverse lithography technique framework, in: IEEE 15th International Conference on ASIC, 2023, pp. 1–4.

[4] T. Fuhner, A. Erdmann, Improved mask and source representations for automatic optimization of lithographic process conditions using a genetic algorithm, Proc. SPIE 5754 (2005) 415–426.

[5] A. Poonawala, P. Milanfar, Mask design for optical microlithography—an inverse imaging problem, IEEE Trans. Image Process 16 (3) (2007) 774–788.

[6] X. Ma, G.R. Arce, Pixel-based OPC optimization based on conjugate gradients, Opt. Express 19 (3) (2011) 2165–2180.

[7] X. Ma, Z. Wang, Y. Li, G.R. Arce, L. Dong, J. Garcia-Frias, Fast optical proximity correction method based on nonlinear compressive sensing, Opt. Express 26 (11) (2018) 14479–14498.

[8] Y. Shen, N. Wong, E.Y. Lam, Level-set-based inverse lithography for photomask synthesis, Opt. Express 17 (26) (2009) 23690–23701.

[9] Y. Shen, N. Jia, N. Wong, E.Y. Lam, Robust level-set-based inverse lithography, Opt. Express 19 (6) (2011) 5511–5521.

[10] Y. Shen, Lithographic source and mask optimization with narrow-band level-set method, Opt. Express 26 (8) (2018) 10065–10078.

[11] X. Ma, X. Zheng, G.R. Arce, Fast inverse lithography based on dual-channel model-driven deep learning, Opt. Express 28 (14) (2020) 20404–20421.

[12] N. Jia, A.K. Wang, E.Y. Lam, Regularization of inverse photomask synthesis to enhance manufacturability, Proc. SPIE 7520 (2009) 112–122.

[13] X. Ma, G.R. Arce, Binary mask optimization for inverse lithography with partially coherent illumination, J. Opt. Soc. Am. A 25 (2008) 2960–2970.

[14] Z. Geng, Z. Shi, X. Yan, K. Luo, Regularized level-set-based inverse lithography algorithm for IC mask synthesis, J. Zhejiang Univ.-SCI. c. 14 (2013) 799–807.

[15] X. Ma, Z. Song, Y. Li, G.R. Arce, Block-based mask optimization for optical lithography, Appl. Opt. 52 (14) (2013) 3351–3363.

[16] S. Osher, R.P. Fedkiw, Level Set Methods and Dynamic Implicit Surfaces, Springer, New York, 2002.

[17] Y. Shen, Level-set based mask synthesis with a vector imaging model, Opt. Express 25 (18) (2017) 21775–21785.

[18] J. Barzilai, J.M. Borwein, Two-point step size gradient methods, IMA J. Numer. Anal. 8 (1) (1988) 141–148.

[19] W. Lv, S. Liu, Q. Xia, X. Wu, Y. Shen, E.Y. Lam, Level-set-based inverse lithography for mask synthesis using the conjugate gradient and an optimal time step, J. Vac. Sci. Technol. B 31 (4) (2013) 041605.

[20] T. Li, Z. Wan, New adaptive barzilai–borwein step size and its application in solving large-scale optimization problems, Anziam J. 61 (1) (2019) 76–98.

[21] S. Huang, Z. Wan, A new nonmonotone spectral residual method for nonsmooth nonlinear equations, J. Comput. Appl. Math. 313 (2017) 82–101.

[22] C. Mack, Fundamental Principles of Optical Lithography: The Science of Microfabrication, John Wiley and Sons, 2007.

[23] X. Ma, Y. Li, Resolution enhancement optimization methods in optical lithography with improved manufacturability, J. Micro/ Nanolith. MEMS MOEMS 10 (2) (2011) 023009.

[24] S. Banerjee, Z. Li, S.R. Nassif, ICCAD-2013 CAD contest in mask optimization and benchmark suite, IEEE/ACM International Conference on Computer-Aided Design 271–274 (2013).

[25] K.F. Chan, Z.Q. Feng, R. Yang, A. Ishikawa, W.H. Mei, High-resolution maskless lithography, J. Micro/nanolithogr., MEMS, MOEMS 2 (4) (2003) 331–339.

[26] K.J. Zhong, Y.Q. Gao, F. Li, Maskless lithography based on DMD, Key Eng. Mater. 552 (2013) 207–213.

[27] J.H. Liu, J.B. Liu, Q.Y. Deng, J.H. Feng, S.L. Zhou, S. Hu, Intensity modulation based optical proximity optimization for the maskless lithography, Opt. Express 28 (1) (2020) 548–557.

[28] Z. Shi, Y. Gao, Fast imaging algorithm for DMD-based photolithography with partially coherent illumination, Optik 123 (18) (2012) 1640–1645.

[29] X. Ma, C. Huang, F. Wang, G.R. Arce, "Model-driven inverse lithography via hypergraph convolutional neural networks and its experimental demonstration", Submitted to, Opt. Laser Technol. (2024).

[30] Z. Xiong, H. Liu, R.H. Chen, J. Xu, Q.K. Li, J.H. Li, W.J. Zhang, Illumination uniformity improvement in digital micromirror device based scanning photolithography system, Opt. Express 26 (14) (2018) 18597–18607.